Available online at www.sciencedirect.com

ScienceDirect

journal homepage: www.elsevier.com/locate/he

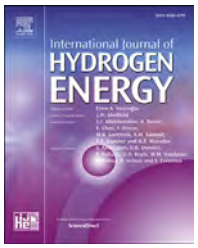

Numerical study of cold start performance of proton exchange membrane fuel cell with coolant circulation

Lin Wei [a], *Zihao Liao* [a,b], *Zhenbang Suo* [c], *Xuesong Chen* [c], *Fangming Jiang* [a,*]

[a] *Laboratory of Advanced Energy Systems, CAS Key Laboratory of Renewable Energy, Guangzhou Institute of Energy Conversion, Chinese Academy of Sciences (CAS), Guangzhou, 510640, China*

[b] *University of Chinese Academy of Sciences, Beijing, 100049, China*

[c] *SAIC Motor Corporation Limited, Shanghai, 201804, China*

HIGHLIGHTS

- A multi-disciplinary cold start model considering coolant circulation is built up.
- The model enables the study of coolant circulation effects on fuel cell cold start.
- The coolant flow rate and total capacity affect the cell cold start performance.
- At lower startup temperature the coolant circulation effects are more obvious.

ARTICLE INFO

Article history:
Received 11 January 2019
Received in revised form
17 May 2019
Accepted 24 June 2019
Available online 17 July 2019

Keywords:
Proton exchange membrane fuel cell
Cold start
Coolant
Numerical model

ABSTRACT

It has been well recognized that cold start is one of the key issues of proton exchange membrane fuel cell (PEMFC) used as the engine of vehicles. Coolant circulation is usually launched synchronously with the fuel cell during cold start to avoid sudden large temperature variation, which greatly increases the cell thermal mass, lowers the heating rate, and worsens the cell performance. Considering the flow and heat transfer of coolant circulation, a three-dimensional, transient, multi-disciplinary model for cold start is built up. The numerical results agree reasonably well with experimental data, indicating that the model can be used for the investigation of PEMFC cold start processes. The analysis of circulation parameter effects shows that increasing the coolant flow rate or coolant tank capacity has little influence on the cell voltage, but will increase the non-uniformity of temperature distribution along flow direction. At lower start-up temperature, this non-uniformity is more obvious. With higher coolant flow rate, although the distribution of current density becomes more evenly, the ice formation amount increases and its distribution and location are greatly affected.

Abbreviations: BP, Bipolar plate; CC, Cooling channel; CFD, Computational fluid dynamics; CL, Catalyst layer; GC, Gas channel; GDL, Gas diffusion layer; LPM, Liter per minute; MEA, Membrane electrode assembly; MPL, Micro-porous layer; PEM, Proton exchange membrane; PEMFC, Proton exchange membrane fuel cell; SIMPLE, Semi-implicit method for pressure linked equation; UDF, User defined functions.

* *Corresponding author.*
E-mail address: fm_jiang2000@yahoo.com (F. Jiang).

https://doi.org/10.1016/j.ijhydene.2019.06.147

Nomenclature

A	area, m^2
a	effective specific area in catalyst layer, m^{-1}
C	molar concentration, mol m^{-3}
c_p	specific heat at constant pressure, J kg^{-1} K^{-1}
D	diffusion coefficient, m^2 s^{-1}
F	Faraday constant, 96,485C mol^{-1}
h	latent heat, J kg^{-1}
I	current density load, A m^{-2}
i_0	exchange current density, A m^{-2}
j	volumetric reaction current density, A m^{-3}
K	permeability, m^2
k	thermal conductivity, W m^{-1} K^{-1}
M	molecular weight, kg mol^{-1}
n	number of electrons in electrochemical reaction; Bruggeman exponent
n_d	electro-osmotic drag coefficient
p	pressure, Pa
R	universal gas constant, 8.314 J mol^{-1} K^{-1}
S	source term in transport equation
s	ice fraction; stoichiometry coefficient in electrochemical reaction
T	temperature, K
U_o	equilibrium cell potential, V
u	fluid velocity, m s^{-1}
V	volume, m^3

Greek characters

α	transfer coefficient
ε	porosity
η	overpotential, V
κ	ionic conductivity, S m^{-1}
λ	water content per sulfonic acid residue, mol H_2O/mol $SO3^-$
μ	viscosity, Pa s
ξ	stoichiometry flow ratio
ρ	density, kg m^{-3}
σ	electronic conductivity, S m^{-1}
τ	shear stress, N m^{-2}
Φ	potential, V

Subscripts

a	anode
c	cathode
e	electrolyte
k	species index
ref	reference value
s	solid, ice
w	water

Introduction

To reduce air pollution, hydrocarbon-free electrified vehicles are becoming a mainstream trend of automobile industry. Lithium-ion battery driven electric vehicles have been widely deployed around the world, though some drawbacks like insufficient battery capacity and long charging time exist [1–3]. The proton exchange membrane fuel cell (PEMFC), which can be filled up with hydrogen in 3–5 min, is a promising clean power for future automotive applications with high fuel-to-energy conversion ratio. However, cold start (i.e., to start the PEMFC from below 0 °C environment) is one of the most key issues to be resolved before widespread application of PEMFC vehicles [4]. During cold start, the mass transfer resistance due to ice formation/presence and the microstructural damage caused by volume expansion during freezing/thawing will not only degrade electrode performances, but also decrease service life of the fuel cell.

A successful cold start depends greatly on the competitive relation between water freezing and temperature rise, which is affected mainly by material properties and operating parameters, such as water transport properties [4–6], start-up temperature [7–11], purge method [12–14], thermal mass [15–17], and loading strategy [18–21]. If a fuel cell has a water storage potential high enough to prevent the three-phase interface from being completely covered by the ice formed, while the temperature rises rapidly to zero degree Celsius, then the cell could start up successfully.

One important parameter influencing the cold start ability of PEMFC is the cell thermal mass. During cold start or at normal operations, the cell thermal mass increased by the coolant circulation ensures that the heat is distributed more uniformly throughout the stack [22]. The deactivation of the cooling circuit during cold start may result in stack degradation due to inhomogeneous temperature distribution and even hot spots in the stack [14]. However, it will also increase the difficulty to start up successfully. Experimental investigation by Schieβwohl et al. [14] shows that reducing the thermal mass of the cooling circuit by two-thirds halves the stack startup time. Besides, at the inlet, temperature decrease caused by coolant flow may cause sudden condensation and additional gas diffusion resistance [23]. The coolant could also be pre-heated above 0 °C by external heating to assist a rapid start-up [16,24].

In order to explore the multi-disciplinary coupling processes during cold start of PEMFC, many models have been developed. Fuel cell models can be generally categorized into lumped 0D or 1D models and 2D/3D CFD (computational fluid dynamics) models [25]. Sundaresan and Moore [22] developed a 1D layered thermal model, in which each cell in a stack was taken as one layer of uniform parameter, to reveal the effects of the endplate's thermal mass. Khandelwal et al. [16] modeled the convective heat transfer of gas/coolant flow in their 1D stack thermal model to account for the heat uptake by coolant with time-dependent coolant inlet temperature. In the system simulation by Tang et al. [23], the stack model with spatial

resolution in two directions was proposed to study the two-phase effects in cold start. To investigate the detailed freezing mechanism inside the catalyst layer, the 2D/3D CFD method was applied. Meng [7] and Jiang et al. [26] developed non-isothermal numerical models to elucidate the interactions of water flow with heat transport. Yang et al. [6] and Yao et al. [27] proposed CFD models considering the supercooled water mechanism to show its effects on the dynamic performance of PEMFC. While detailed temperature distribution inside a cell was demonstrated, the effects of coolant on heat transfer is not included in those models. In the numerical investigation by Ko et al. [15], the cold start performances were compared between empty cooling channel and the one filled with coolant. The startup time of PEMFC with cooling channel filled with coolant is almost twice longer than the other counterpart even without considering the slower temperature rise rate caused by the flow circulation of coolant.

Although many cold start researches have been conducted for PEMFC thermal analysis, the coolant circulation effects on the cold start performance has not yet been investigated. This study focuses on the flow rate and total capacity of coolant circulation to investigate their effects on thermal mass and temperature distribution inside the fuel cell. A multi-disciplinary coupling numerical model with built-in cooling channels is developed to simulate the coolant flow and heat transfer. The relationship between the cell temperature distribution and coolant circulation parameters is analyzed. Besides, the effects on current density and ice distribution are discussed.

Mathematical model

Fig. 1 shows the basic working principle of PEMFC. Bipolar plate (BP), cooling channel (CC), gas channel (GC), gas diffusion layer (GDL), micro-porous layer (MPL), catalyst layer (CL) and proton exchange membrane (PEM) are main regions of a PEMFC. The subzero temperature self-start process takes advantage of the heat generated by electrochemical reactions and ohmic transport of anode and cathode to warm the fuel cell, until the temperature reaches 0 °C and the output power rises to the target value. The coolant used is the glycol coolant, which is stored in the coolant tank. The coolant circulation is launched synchronously with the cell cold start operation. A circulation with low flux instead of static coolant could avoid unexpected hot spots as well as temperature drop when the low temperature coolant suddenly flows into the cell.

The present multi-disciplinary numerical model is formulated based on the governing equations of mass, momentum, species, charge and energy conservation laws as well as electrochemical reactions to simulate the multi-transport and electrochemical process occurring in the interior of this fuel cell.

Model assumptions

Based on the characteristics of a cell starting up from subzero temperature and properties of macro-scale multiple transfer, some basic assumptions are made [28]. The fluid is assumed to be an incompressible ideal gas mixture. The special pore-structure of MPL is assumed to have no additional influence on PEMFC cold start and it is thus combined with the GDL [26]. The porous layer (GDL/CL) is considered as isotropic and homogeneous. It is also assumed that when the vapor reaches saturation, it will instantaneously sublimate. For the coolant circulation, the coolant is assumed to be evenly distributed to each single cell from the manifold. After the coolant flows from the outlet, the mixing with coolant in the coolant tank is assumed to be very soon that the temperature is uniform in the coolant tank.

Governing equations

The governing equations and source terms for PEMFC cold start [26] are summarized in Tables 1 and 2, respectively.

The flow field is determined by mass and momentum conservation equations. In mass continuity equation, there is no source term since the influence of the consumption/formation of reactants/products on the flow characteristics is negligible [29]. For flow in open channels, i.e. GC and CC, there is no source in momentum equation while for that in porous media, GDL and CL, the drag force on fluid by solid matrix is given as $S_u = -\frac{\mu}{K}\mathbf{u}$.

The general species conservation equation for H_2, O_2, vapor, and water content in ionomer are given in terms of molar concentration. The species source term $S_{C,k} = -\frac{s_{kj}}{nF}$ represents a source/sink in CLs arising from electrochemical reactions, which is proportional to volumetric current density j. In addition, the effects of electro-osmotic drag on water transport in PEM and CL and the source term due to phase change are considered in the water source term. The phase change source is given as:

$$S_{ice} = \begin{cases} 0, & C^{H_2O} \le C_{sat}^{H_2O} \\ r_{freeze}\left(C_{sat}^{H_2O} - C^{H_2O}\right), & C^{H_2O} > C_{sat}^{H_2O} \quad \text{and } T < T_{freeze}^{H_2O} \\ r_{melt}\left(C_{sat}^{H_2O} - C^{H_2O}\right), & T = T_{freeze}^{H_2O} \quad \text{and } s > 0 \\ 0, & T \ge T_{freeze}^{H_2O} \quad \text{and } s = 0 \end{cases} \tag{1}$$

To account for the effects of porosity and tortuosity of porous layers (GDL/CL), the effective species diffusion coefficient D_k^{eff} in the above equation is modified via Bruggeman correlation as follows:

$$D_k^{eff} = D_k \varepsilon^n \tag{2}$$

The Bruggeman index related to tortuosity is usually set as $n = 1.5$. The blockage of species diffusion caused by ice formation can be simply corrected by ice fraction s, that is:

$$D_k^{eff} = D_k[\varepsilon(1-s)]^n \tag{3}$$

The source terms of electrolyte and electron phase given in the charge conservation equations have equal absolute value, indicating the sum of current flow by protons and by electrons are constant and always equal to the applied current loading. Based on Butler-Volmer equation, the electrochemical-reaction kinetics for anode and cathode reactions in CL can be given by

$$j_a = a i_{0,ref}^{H_2} \left(\frac{C^{H_2}}{C_{ref}^{H_2}}\right)^{1/2} \exp\left(\frac{\alpha_a + \alpha_c}{RT} F\eta\right) \tag{4}$$

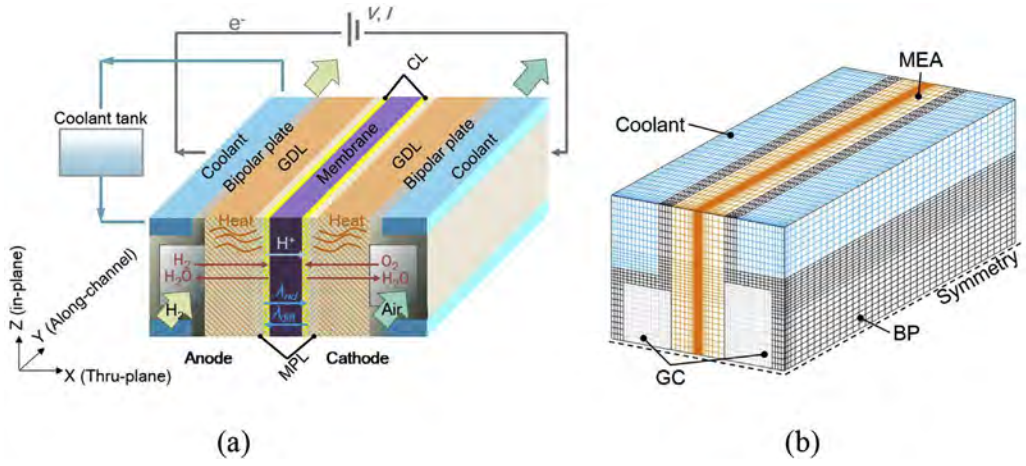

Fig. 1 – Schematic (a) and computational domain (b) of the PEMFC.

$$j_c = -ai_{0,ref}^{O_2}\frac{C^{O_2}}{C_{ref}^{O_2}}\exp\left(-\frac{\alpha_c}{RT}F\eta\right) \tag{5}$$

where the surface overpotential η is defined as

$$\eta = \phi_s - \phi_e - U_0 \tag{6}$$

In the energy conservation equation, heat source term may contain the entropic heat, irreversible electrochemical heat, ohmic heat and latent heat.

Calculation of coolant circulation

The mass, momentum and energy conservation equations are solved for coolant in CC. No external heating is considered in this model, and the coolant is warmed up by the heat generated in PEMFC itself.

According to the coolant flow distribution assumption, the coolant flow rate for single cell can be simply calculated by dividing the coolant flow rate of the stack by the number of cells $\left(\dot{V}_{singlecell} = \frac{\dot{V}_{stack}}{n_{cell}}\right)$.

The coolant in CC as well as the coolant in tank increases the total thermal mass of PEMFC which is manifested in the mixing process. The coolant from the outlet is firstly mixed with the coolant in the tank, and then is pumped back to the coolant inlet. The tank temperature change during mixing is calculated as

$$T_{coolant,tank} = \frac{T'_{coolant,out}\dot{V}_{coolant}\Delta t + T'_{coolant,tank}V_{tank}}{\dot{V}_{coolant}\Delta t + V_{tank}} \tag{7}$$

where the $T'_{coolant,out}$ and $T'_{coolant,tank}$ are the outlet and the tank temperature in the previous time step, $\dot{V}_{coolant}$ the volume flow rate of coolant and Δt the time step.

Table 1 – Governing equations for PEMFC cold start model.

	Governing equations
Mass	$\frac{\partial(\varepsilon_s\rho_s)}{\partial t} + \frac{\partial(\varepsilon\rho)}{\partial t} + \nabla\cdot(\rho\boldsymbol{u}) = 0$
Momentum	$\frac{1}{\varepsilon}\left[\frac{\partial(\rho\boldsymbol{u})}{\partial t} + \frac{1}{\varepsilon}\nabla\cdot(\rho\boldsymbol{u}^2)\right] = -\nabla p + \nabla\cdot\tau + S_u$
Species	$\frac{\partial(\varepsilon C_k)}{\partial t} + \nabla\cdot(\boldsymbol{u}C_k) = \nabla\cdot(D_k^{eff}\nabla C_k) + S_{C,k}$
Charge	$0 = \nabla\cdot(\kappa^{eff}\nabla\phi_e) + S_{\phi,e}$ $0 = \nabla\cdot(\sigma\nabla\phi_s) + S_{\phi,s}$
Energy	$\frac{\partial(\rho c_p T)}{\partial t} + \nabla\cdot(\rho c_p \boldsymbol{u}T) = \nabla\cdot(k^{eff}\nabla T) + S_T$

Boundary and initial conditions

The 3D computational domain considered in this work is displayed in Fig. 1(b). The cooling channel on the shoulder of BP at both sides is devised in our model. Due to the symmetrical structure, only half of the single cell with straight flow channel is built to shorten the computational time.

The hydrodynamic boundary conditions for GC and CC are to specify velocity and pressure (relative) at the inlet and the outlet, respectively. The velocity of the coolant inlet is given in terms of the pump flow rate. The velocity in GC is determined by reference current density, I, and stoichiometric ratio, ξ, as follows:

$$u_{in,a} = \frac{\xi_a\frac{I}{2F}A_{PEM}}{C_{H_2}A_{a,GC}}, \quad u_{in,c} = \frac{\xi_c\frac{I}{4F}A_{PEM}}{C_{O_2}A_{c,GC}} \tag{8}$$

At the inlet of GC, the concentration values for H_2 and O_2 are set as constant, and zero for vapor under the assumption of that the inlet gas is dry. The temperature of the inlet gas is equal to that of the environment. The coolant inlet temperature is the same as that of the coolant in tank as given by Eq. (7).

Equations 9 and 10 give the charge transport boundary conditions. A reference electronic phase potential (zero) is set at the anode side and a constant flux (current density loading) at the cathode wall, so that the calculated electron phase potential on the cathode wall would be the cell output voltage. For the electrolyte phase potential, zero-flux boundary condition is applied on the walls at both sides:

Table 2 – Source terms for PEMFC cold start model.

	GDL	CL	PEM	BP	CC
Mass	0	$S_m = \rho_{ice} S_{ice}$	0	/	0
Momentum	$S_u = -\frac{\mu}{K}\boldsymbol{u}$	$S_u = -\frac{\mu}{K}\boldsymbol{u}$	/	/	0
Species[a]	$S_C = -S_{ice}$	$S_C = -\frac{s_k j}{nF} - \nabla\cdot\left(\frac{n_d}{F}\mathbf{i}_e\right) - S_{ice}$	$S_C = -\nabla\cdot\left(\frac{n_d}{F}\mathbf{i}_e\right)$	/	/
Charge	/	$S_{\phi,e} = j$	0	/	/
	0	$S_{\phi,s} = -j$	/	0	/
Energy	$S_T = \frac{i_s^2}{\sigma} + h_{sg} S_{ice}$	$S_T = j\left(\eta - T\frac{dU_0}{dT}\right) + \frac{i_e^2}{\kappa^{eff}} + \frac{i_s^2}{\sigma} + h_{sg} S_{ice}$	$S_T = \frac{i_e^2}{\kappa^{eff}}$	$S_T = \frac{i_s^2}{\sigma}$	0

[a] The electro-osmotic term is only applied for water in ionomer phase, and S_{ice} is for H_2O transport only.

$$(\phi_s)_{anode\ wall} = 0, \quad \left(\frac{\partial \phi_s}{\partial n}\right)_{cathode\ wall} = I \tag{9}$$

$$\left(\frac{\partial \phi_e}{\partial n}\right)_{wall} = 0 \tag{10}$$

All the other external boundaries are assumed to be zero-flux for all the other main variables not mentioned above.

The initial temperature for the whole PEMFC is set as that of the environment. The reactant species in GCs and GDLs are initially set to have the same molar concentration as the inlet gas. Before cold start, it is assumed that a sufficiently long purge with gas of 50% relative humidity has been performed that the initial water content in ionomer phase and in PEM is $\lambda_0 = 3.3$ [30], and the initial ice fraction in the cell is assumed zero [31].

The cell dimensions and material properties are listed in Tables 3 and 4, respectively. The proton conductivity in the membrane, κ, and the water diffusion coefficient in the membrane, D_w^m, are given by Eq. (11) [32] and Eq. (12) [33], respectively.

$$\kappa = \exp\left[2222\left(\frac{1}{303} - \frac{1}{T}\right)\right](0.5139\lambda - 0.326) \tag{11}$$

$$D_w^m = \begin{cases} 3.1\times10^{-7}\lambda\left(-1+e^{0.28\lambda}\right)\left(e^{\frac{-2436}{T}}\right), & 0<\lambda<3 \\ 4.17\times10^{-8}\lambda(1+161e^{-\lambda})\left(e^{\frac{-2436}{T}}\right), & \text{otherwise} \end{cases} \tag{12}$$

Mesh and numerical procedure

A structured grid as displayed in Fig. 1(b) was applied, and a finer grid was used in the thin region of membrane electrode assembly (MEA) where the reactions take place. The conservation equations along with the boundary conditions and initial conditions are solved using the commercial CFD flow solver, Fluent©. By customizing its user defined functions (UDFs), we implemented the various source terms, physical properties, diffusion terms and non-standard advection–convective terms in the governing equations. The well-known SIMPLE (semi-implicit method for pressure linked equation) algorithm is used to address the pressure–velocity coupling and the first order upwind differencing scheme is generally used for discretization of the velocity field. The influence of grid number on calculation result was examined in advance to ensure its grid-independence. Table 5 compares the cell voltage calculated using meshes of different grid number. As grid number increases, the value of cell voltage gradually reaches to an asymptotic value and the error compared to the finest mesh (Mesh 5) decreases. Mesh 3 with a numerical error less than 3% is used for model calculations to save the computation time with no significant compromise at the calculation accuracy.

Validation

Comparison with experimental data

The present model predictions were compared with the experimental results for the cold start process at −20 °C [34], as shown in Fig. 2. The experiments were carried out in SAIC Motor with respect to a real PEMFC engine. The experimental setup for cold start of the cell stack contains a PEMFC stack, a climate chamber, an electronic load and sensors. The test rig was put in the −20 °C climate chamber for 24 h to make sure the temperature the stack inside drops to −20 °C. H_2 was supplied by a high pressure hydrogen bottle and its pressure and flow rate was controlled by a decompressor. A compressor was used to feed air into the fuel cell stack.

In the experiments, the current loading increases gradually to keep lower output power, and in the model, a step-loading with approximately the same loading rate as the experiment is applied. The coolant initial temperature is set as −17 °C, the

Table 3 – Cell dimensions.

Description	Value
Cell length	0.28 m
Width of anode/cathode GC	0.9/1.2 mm
Width of anode/cathode CC	1.1/0.8 mm
Depth of GC	0.4 mm
Thickness of BP (δ_{BP})	0.1 mm
Thickness of GDLs (δ_{GDL})	0.2 mm
Thickness of CLs (δ_{CL})	0.015 mm
Thickness of PEM (δ_{PEM})	0.018 mm

Table 4 – Material properties.

Description	Value	Units
Porosity of GDL/CL ($\varepsilon_{GDL}/\varepsilon_{CL}$)	0.51/0.40	
Permeability of the GDL/CL (K_{GDL}/K_{CL})	6.1×10^{-12}	m^2
Electronic conductivity in BP (σ_{BP})	1.4×10^{6}	$S\ m^{-1}$
Electronic conductivity in GDL/CL (σ_{GDL}/σ_{CL})	300	$S\ m^{-1}$
Thermal conductivity of BP (k_{BP})	16	$W\ m^{-1}\ K^{-1}$
Thermal conductivity of GDL/CL (k_{GDL}/k_{CL})	1.7/0.27	$W\ m^{-1}\ K^{-1}$
Thermal conductivity of PEM (k_{PEM})	0.16	$W\ m^{-1}\ K^{-1}$
Thermal conductivity of coolant ($k_{coolant}$)	0.25	$W\ m^{-1}\ K^{-1}$
Thermal mass of BP ($\rho c_{p,BP}$)	4000	$kJ\ m^{-3}\ K^{-1}$
Thermal mass of GDL/CL ($\rho c_{p,GDL}/\rho c_{p,CL}$)	230/580	$kJ\ m^{-3}\ K^{-1}$
Thermal mass of PEM ($\rho c_{p,PEM}$)	2300	$kJ\ m^{-3}\ K^{-1}$
Thermal mass of coolant ($\rho c_{p,coolant}$)	3400	$kJ\ m^{-3}\ K^{-1}$
Diffusivity of H_2/O_2 in gas (D_{H2}/D_{O2})	$8.67 \times 10^{-5}/1.53 \times 10^{-5}$	$m^2\ s^{-1}$
Diffusivity of vapor in gas (D_{vapor})	1.79×10^{-5}	$m^2\ s^{-1}$
Dry membrane density (ρ_{PEM})	1980	$kg\ m^{-3}$
Equivalent weight of electrolyte in PEM (EW)	1.0	$kg\ mol^{-1}$

same as the experimental. It can be noted that the model predictions for the cell voltage agrees well with the experimental data. In the loading phase, the cell voltage predicted by the model is higher than the tested, which is because that the current density applied in the model is lower than that in the experiments. When the current density remains constant, the predicted cell voltage is less than the tested with a relative deviation less than 6%. This deviation can be explained with the temperature results shown in Fig. 2(b). The calculated coolant inlet temperature increases in accordance with the experimental curve. For the coolant outlet temperature, both experimental and simulated curves show a flat stage first and then they keep rising later on. The calculated coolant outlet temperature curve shows almost the same rising rate with the experimental value, while there is about 6 °C temperature difference between the two curves. This temperature difference can be ascribed to the additional thermal mass of fluid manifold/distributer and the heat transfer resistance of the real PEMFC engine, which are not considered in the simulation. The comparison results indicate that the model could give a reasonable prediction of PEMFC cold start performances.

Heat and water balance

In the present model, many parameters, such as reaction intensity, diffusivity, proton conductivity and saturation value of vapor, are functions of temperature; the temperature field is influenced by current density and proton conductivity. Therefore, getting a converged solution is challenging. The water transfer is a complicated multiphase yet important equilibrium process since it contains vapor diffusion, water diffusion in ionomer, electro-osmosis and freezing.

Table 5 – Grid-independence check.

	Grid number	$I = 1200\ A/m^2$, $\lambda_0 = 3$		$I = 1200\ A/m^2$, $\lambda_0 = 5$	
		Cell voltage (V)	Error	Cell voltage (V)	Error
Mesh 1	24,640	0.5028	5.8%	0.4679	6.8%
Mesh 2	56,700	0.5212	3.6%	0.4868	3.9%
Mesh 3	**89,320**	**0.5298**	**2.0%**	**0.4953**	**2.2%**
Mesh 4	136,160	0.5361	0.9%	0.5018	0.9%
Mesh 5	179,450	0.5408	/	0.5064	/

The total heat generation is composed of irreversible reaction heat, ohmic heat, entropic heat and latent heat. By integrating the heat source terms over the entire cell, various heat generation rates are obtained. Heat generation rates as functions of time are shown in Fig. 3(a). Note that the heat generation values have been divided by the BP side surface area and therefore has a unit of W/cm^2. It can be seen that except for the latent heat, all other heat generation rates increase with current loading, and the latent heat due to freezing of water begins to appear at around 14 s. The irreversible reaction heat, contributing to about half of the total heat generation, is mainly associated with oxygen reduction reaction and changes slightly if the current load is unchanged. The ohmic heat decreases with time during each current load stage because of the increase of water content and proton conductivity of the membrane. In order to examine the solution of energy conservation equation, the heat absorption rate ($= mc_p/A \cdot dT/dt$) is also integrated over the entire cell and the coolant circulation. Plotted by the scattered points, the heat absorption rate shows good coincidence with the total heat generation rate, indicating the energy conservation equation is well converged.

Fig. 3(b) illustrates the evolution of water production rate and water flow/removal rate. The positive curve shows the total water production rate in PEMFC, which should theoretically be equal to $M_w I/2F$. The other curves are the water accumulation rate in ACL, PEM and CCL, as well as ice formation rate and vapor exhaust rate. Since CCL is where water comes from and PEM has large water storage potential, the water in PEM and CCL accumulates faster than the other regions. On the contrary, the vapor outflow rate is very small due to low saturation pressure. Except for the water stored in CCL, most of the water produced diffuses to PEM and to the anode side, and when the water content reaches saturation at around 14 s, the excess water starts to form ice. At each time point, the sum of water accumulation rate, ice formation rate and vapor outflow rate is balanced with the water

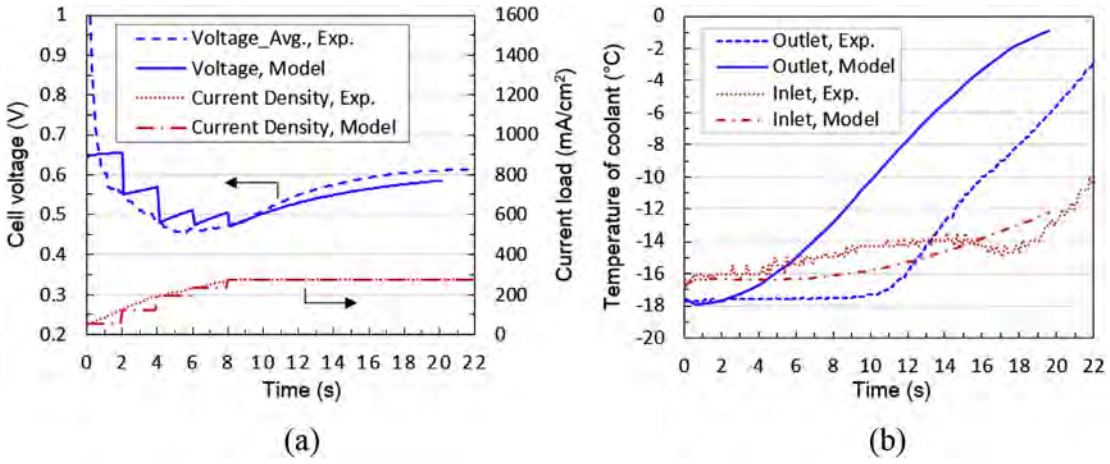

Fig. 2 – Comparison of present model prediction with experimental results. (a) Evolution of cell voltage and current density; (b) Evolution of coolant temperature at inlet and outlet.

production rate, proofing the convergence of water transport equation.

Results and discussion

This section presents a parametric study of effects of coolant flow on PEMFC cold start. The current loading profile is the same as that in Section Comparison with experimental data while the stoichiometry coefficient at the anode and the cathode are 2 and 3, respectively.

Effects of coolant flow rate and coolant capacity on temperature

The flow rate and total mass of coolant are key parameters relevant to coolant circulation. The coolant flow rate could be adjusted by controlling the circulation pump, while the total mass of coolant in the circulation usually depends on the volume of coolant tank (including pipeline of the circuit) which is immutable for a PEMFC system. Under normal conditions, the coolant flow rate is calculated according to the cooling requirement and temperature difference between coolant inlet and outlet $\left(\dot{V}_{coolant} = \frac{Q}{(\rho c \Delta T)_{coolant}}\right)$; the coolant capacity design is affected by the heat dissipation performance. Discussion here only provides some reference for the coolant capacity design in view of cold start. A dimensionless volume ratio is used to represent the total mass of coolant, that is:

$$r_{coolant,V} = \frac{V_{tank} + V_{CC}}{V_{CC}} \tag{13}$$

Cases with different coolant circulation parameter at start-up temperature of −20 °C are compared in Fig. 4. Simulations stop once the cell maximum temperature reaches 0 °C when it is ensured that the PEMFC successfully starts up. According to Fig. 4(a), voltage curve drops slightly when the coolant flow rate increases from 20 LPM (liter per minute) to 80 LPM with

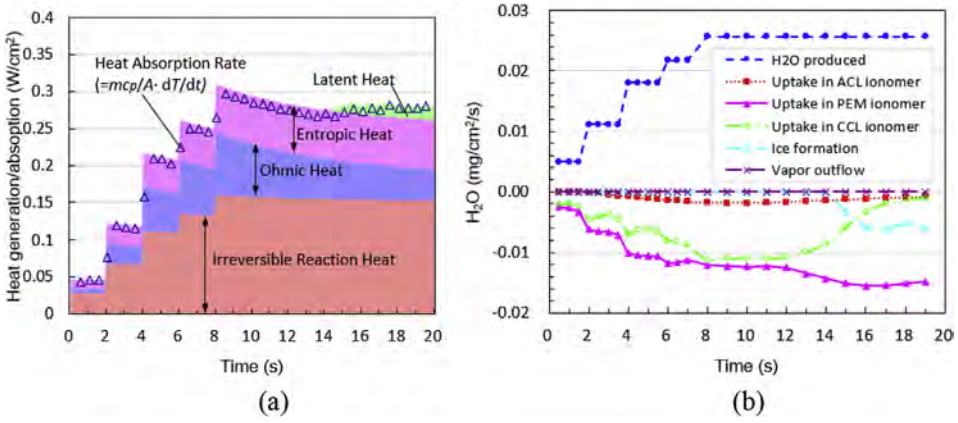

Fig. 3 – Evolution of heat balance and water balance. (a) Heat generation rate of each sources and total heat absorption rate; (b) Water production rate and accumulation rate of each region.

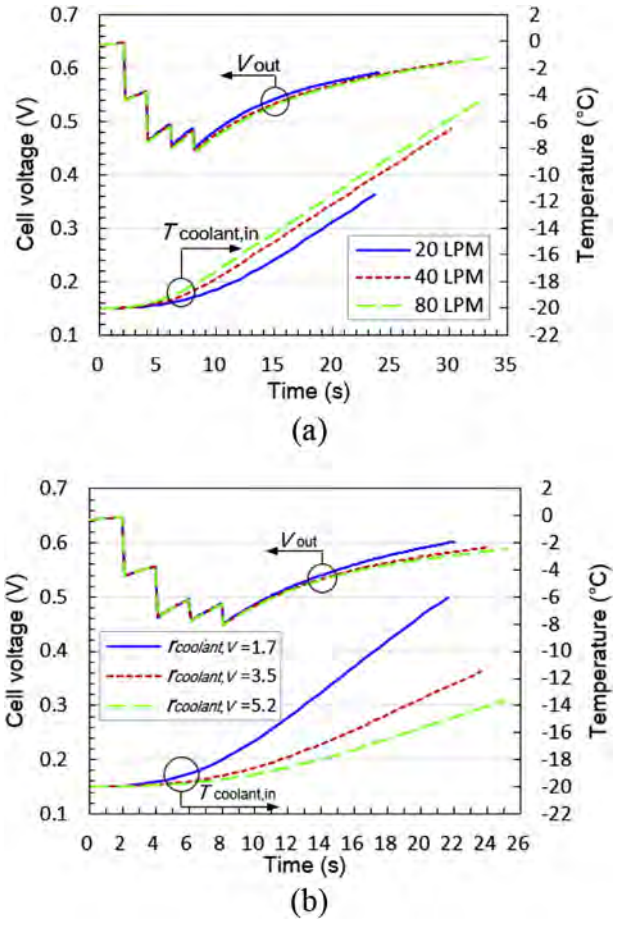

Fig. 4 – Evolution of cell voltage and coolant inlet temperature. (a) Different coolant flow rate; (b) Different coolant capacity.

the same coolant tank volume ($r_{coolant,V} = 3.5$). With 20 LPM, it takes 23.9 s for the cell maximum temperature to reach 0 °C while increasing the flow rate to 80 LPM prolongs this time to 33.2 s. Increasing the coolant flow rate results in more heat to be taken away by the coolant through heat convection. Hence the coolant inlet temperature rises faster, but more time is required to heat up the PEMFC.

The total thermal mass of the coolant increases with the coolant tank capacity. As shown in Fig. 4(b), the coolant inlet temperature rise rate decreases significantly when $r_{coolant,V}$ increases from 1.7 to 5.2. For the three coolant capacity considered here, the cell voltage curves are in a similar trace in the early period, and they diverge as the curve associated with a larger thermal mass has a weaker rising momentum. The three cases stop (meaning the maximum temperature in the cell reaches 0 °C) at 22.0, 23.9, 25.2 s, respectively. As expected, the larger coolant capacity prolongs the start-up process.

Although the effect of coolant flow rate or capacity on the output voltage is small, their influence on temperature distribution is not negligible. Fig. 5 compares the average temperature along y direction of coolant, BP and MEA. The temperature, as seen, increases gradually over time for all the cases. At 1 s, the temperature difference between MEA and coolant, $\Delta T_{coolant,MEA}$, is small, then as constantly heat generated from CCL and PEM, this difference increases to a stable value. Comparing the 20 LPM and 80 LPM cases in Fig. 5(a) and (b), more even temperature distribution along y axis is observed for the latter as a result of faster circulation, which is in accordance with the PEMFC stack performances under normal conditions [35,36]. At 23 s, the temperature difference between the inlet and the outlet portions in MEA, ΔT_{MEA} are 9.7 °C for 20 LPM case, while only 2.9 °C for 80 LPM case. However, with the higher flow rate, as a result of the slower temperature rise rate much more time is needed for the coolant to reach 0 °C. In the comparison of different coolant capacity in Fig. 5(c) and (d), the relative low coolant inlet temperature of $r_{coolant,V} = 5.2$ case leads to more uneven temperature distribution with $\Delta T_{MEA} = 11.8$ °C which is more than twice the value of $r_{coolant,V} = 1.7$ case (4.9 °C). Even though the big difference in coolant inlet temperature, the coolant outlet temperature shows only slight difference between the two cases. The uneven distribution of temperature has a great impact on the performance of PEMFC, which will be detailed in Section Effects on current density and ice distribution.

Effects of ambient temperature

The PEMFC cold start performances are greatly affected by the ambient temperature. At low ambient temperatures, the water diffusivity in ionomer and the proton conductivity of MEA decreases; and much more heat is required for cell temperature to leave the sub-zero range especially with circulating coolant. Hence, it is more difficult to start PEMFC at lower ambient temperatures. The evolution curves of cell voltage and coolant inlet temperature are shown in Fig. 6(a) for different ambient temperatures from −10 to −30 °C. It only takes 12.0 s for the maximum temperature to reach zero for −10 °C case whereas with a lower ambient temperature, i.e. for −30 °C, the time is more than triple, 39.2 s. Similarly, the output voltage is much lower at a lower startup temperature. It can be concluded that the low proton conductivity due to low temperature increases the ohmic loss, so the output voltage ($V_{out} = V_{nerst} - \eta_{act} - \eta_{ohmic} - \eta_{conc}$) decreases significantly. The coolant inlet temperature also increases faster when more Joule heat is generated for the −30 °C case.

The temperature along y axis is shown in Fig. 6(b) and (c). At 11 s, the temperature difference between the inlet and the outlet portion in MEA, ΔT_{MEA}, are 5.7 °C for −10 °C case and 7.4 °C for −30 °C case, while at 37 s this value increases to as much as 10.2 °C for the latter case. This indicates more uneven temperature distribution if the initial startup temperature is lower. On the other hand, the average temperature difference between coolant and MEA, $\Delta T_{coolant,MEA}$, is larger with the −30 °C case hence more heat is taken away by the coolant. At 11 s, the $\Delta T_{coolant,MEA}$ of −10 °C and −30 °C case are 1.2 and 1.4 °C, respectively, as a result, more heat is transferred to the coolant. It could be seen that lowering initial startup temperature boosts the effects of coolant circulation.

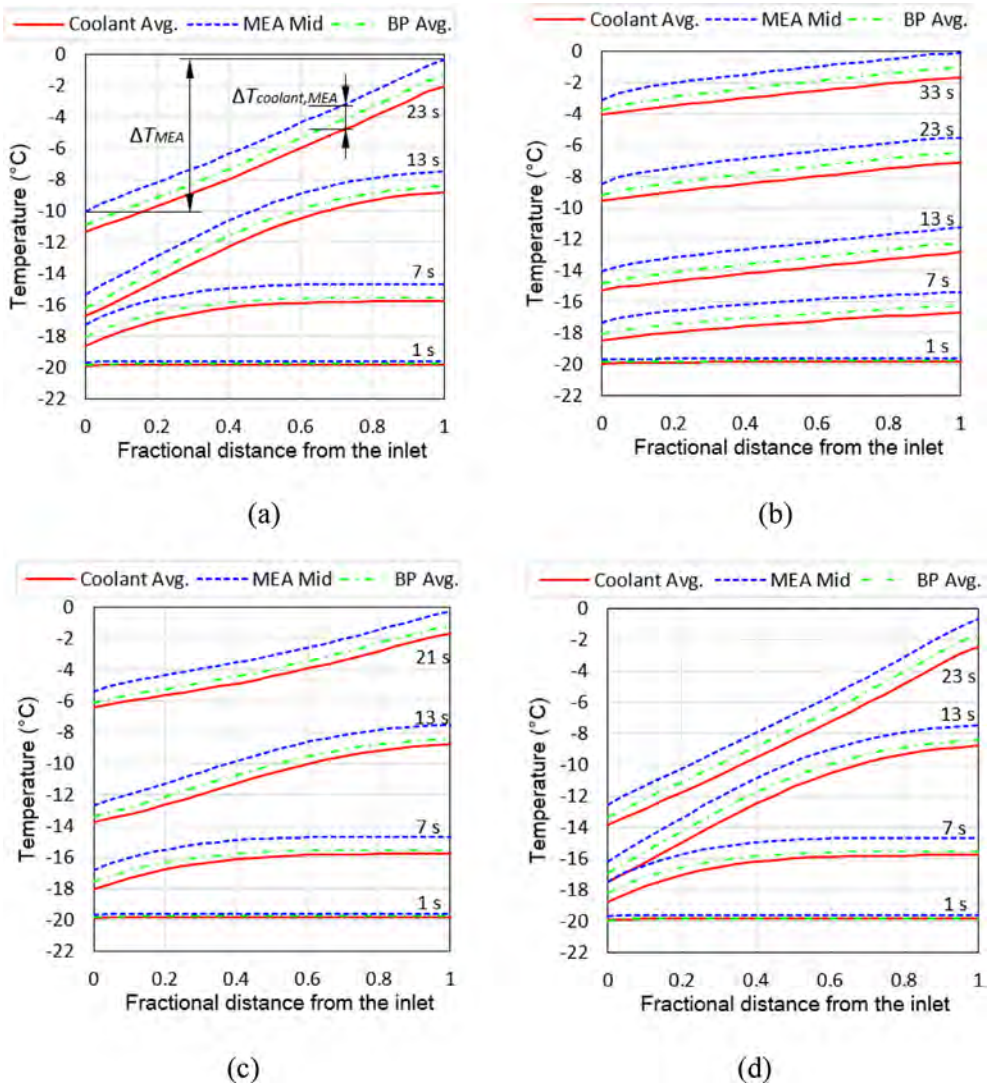

Fig. 5 – Temperature distribution of coolant, MEA and BP along y axis (flow direction). (a) $r_{coolant,V} = 3.5$, 20 LPM; (b) $r_{coolant,V} = 3.5$, 80 LPM; (c) $r_{coolant,V} = 1.7$, 20 LPM; (d) $r_{coolant,V} = 5.2$, 20 LPM.

Effects on current density and ice distribution

As mentioned above, low coolant flow rate of large coolant tank capacity could result in more uneven temperature distribution. The further effects on proton transfer and ice formation are discussed as follows.

Fig. 7 shows the proton current density contour in mid-MEA plane at different time under a start-up temperature of −20 °C. The current loads at 1, 7, and 13 s are 530, 2330, and 2760 A/m^2, respectively. The dashed lines show the rib boundary at anode and cathode sides, which marks off the region under BP and under GC in the MEA. When t = 1 s, for coolant flow rate of both 20 and 80 LPM, the temperature of the whole cell is close to that of the environment, therefore the effects of temperature distribution is negligible while the gas concentration and electron conductivity are dominant factors in determining the reaction intensity distribution. In the region under BP, the electron could transfer directly along *x* axis from GDL to the adjacent BP. Nevertheless, in the region under GC, the GDL is next to the GC rather than the BP so that the electron transfer path is longer than that in the region under BP. Hence the current density is higher in the region under BP due to lower resistance. Along the flow direction, the current density demonstrates a decreasing trend due to the similar distribution of the H_2/O_2 concentration.

The inside temperature of PEMFC increases when the heat being continually generated from the reactions, while the inlet gas temperature still stays at a lower value. For the 20 LPM case, since the mid-MEA temperature increases from inlet to $y \geq 0.5l_{cell}$ with a maximum difference of about 3 °C at 7 s (Fig. 5(c)), the water diffusivity and proton conductivity at $y \geq 0.5l_{cell}$ are higher than the rest region according to Eqns. 11 and 12. Combined with the effects of gas concentration and

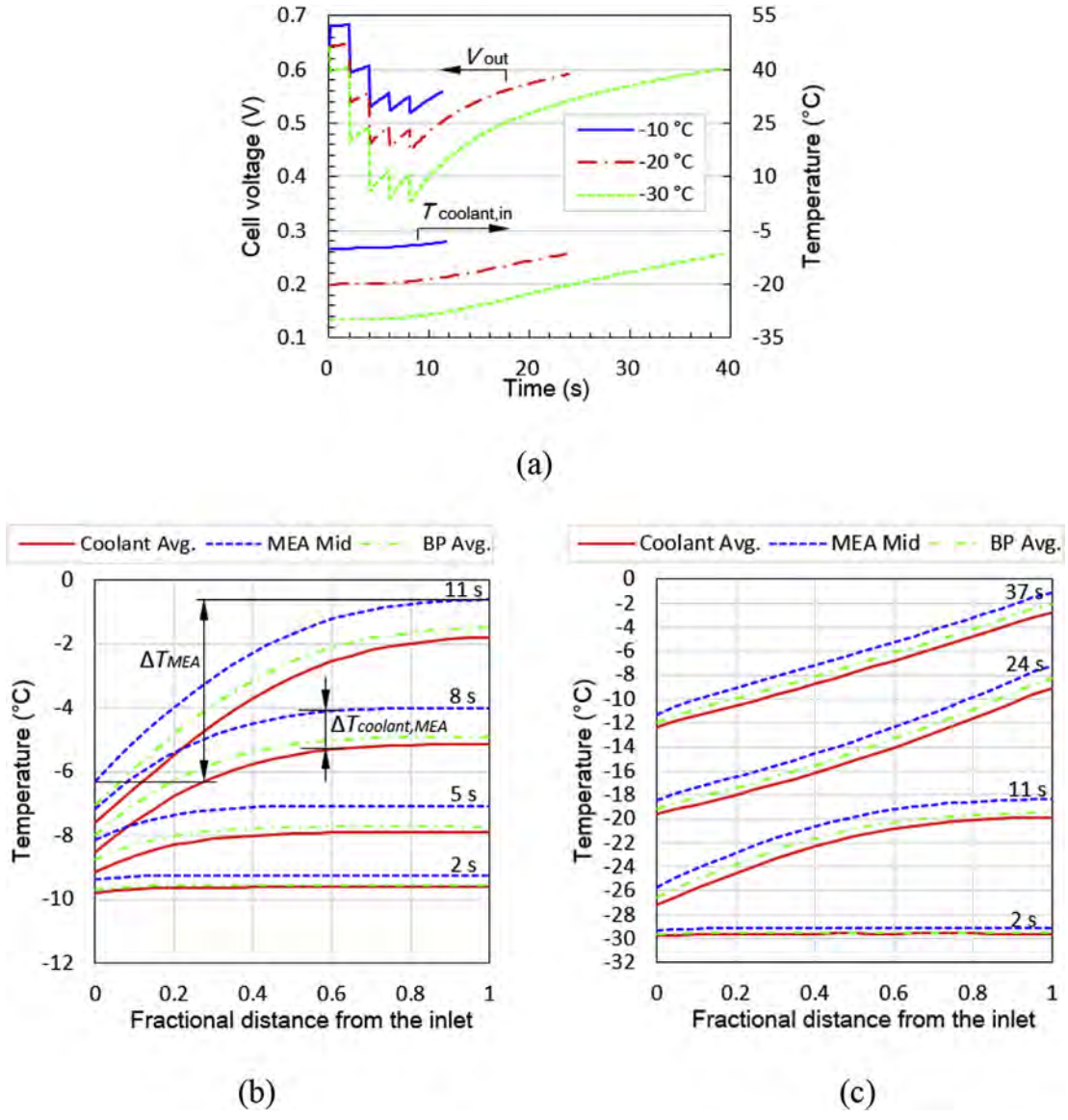

Fig. 6 – Comparison between different start-up temperature. (a) Evolution of cell voltage and coolant inlet temperature; (b) Temperature distribution along flow direction for $T_0 = -10$ °C; (c) Temperature distribution along flow direction for $T_0 = -30$ °C.

electron conductivity, the maximum current density region shifts to the middle from the inlet. With more even temperature distribution, the current density of 80 LPM case likewise shows more uniform distribution along y axis. The difference of current density distribution becomes more pronounced at $t = 13$ s when the maximum current density region is located near the outlet for the 20 LPM case with large gradient, while the current density is still much more evenly distributed for the 80 LPM case.

The ice fraction in CCL in the −20 °C startup temperature case is demonstrated in Fig. 8(a) and (b) for different coolant flow rate. At 23 s, because of the higher water transfer resistance and the larger current density, more ice forms in the region under BP than under GC. Clearly, higher ice fraction is shown for the case with larger coolant flow rate as expected. When the initial startup temperature is as low as −30 °C (see in Fig. 8(c) and (d)), the amount of ice is much more at the whole region and the maximum ice fraction is seen in the region toward the outlet. In comparison with the 20 LPM case, the ice fraction of the 40 LPM case is relatively more evenly distributed along y axis and is larger due to the lower temperature rise rate. The maximum ice location for −30 °C startup temperature cases is apparently different from that for −20 °C cases, indicating the effects of initial startup temperature on water diffusion in MEA are significant. With a lower ambient temperature, more water is accumulating in CCL and especially in the region toward the outlet where reaction is more intense.

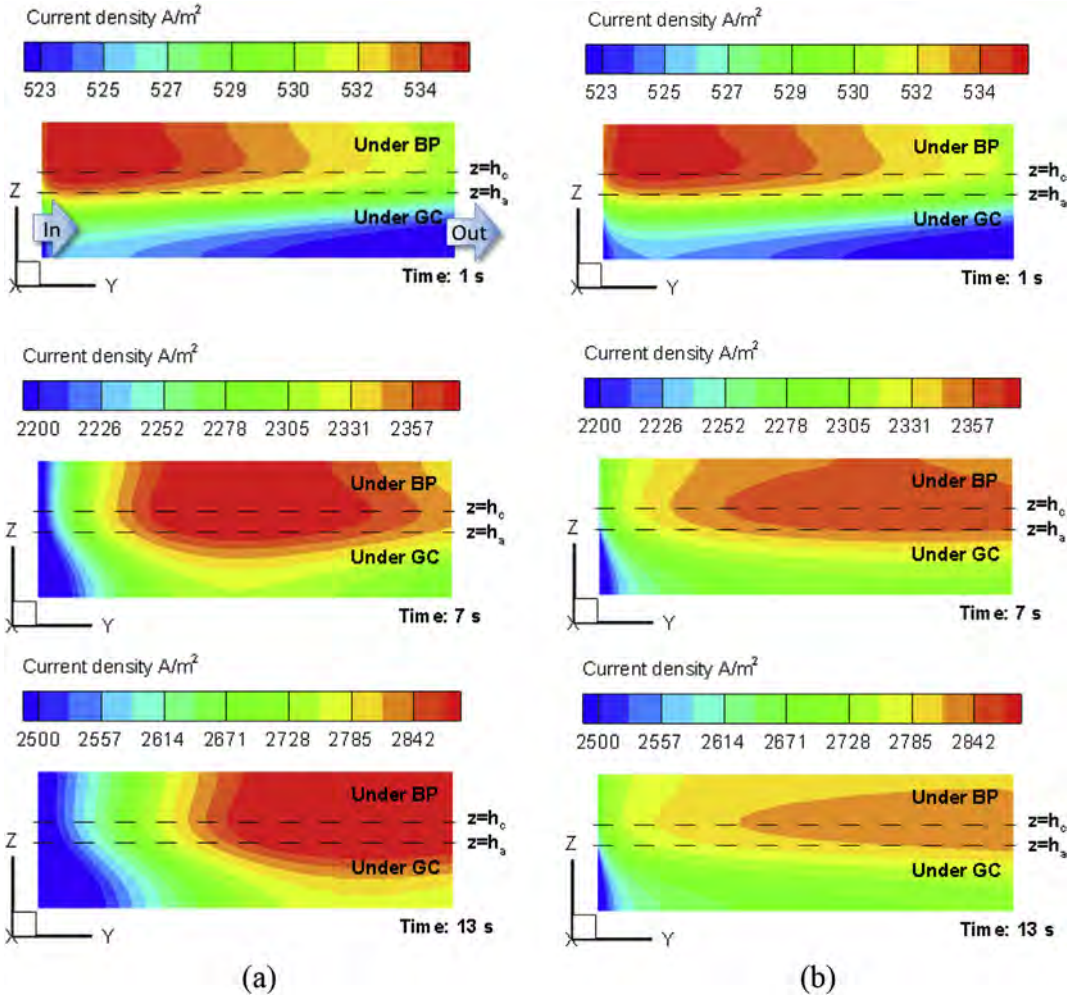

Fig. 7 – Proton current density distribution in mid-MEA (−20 °C) at 1, 7 and 13 s. (a) 20 LPM; (b) 80 LPM.

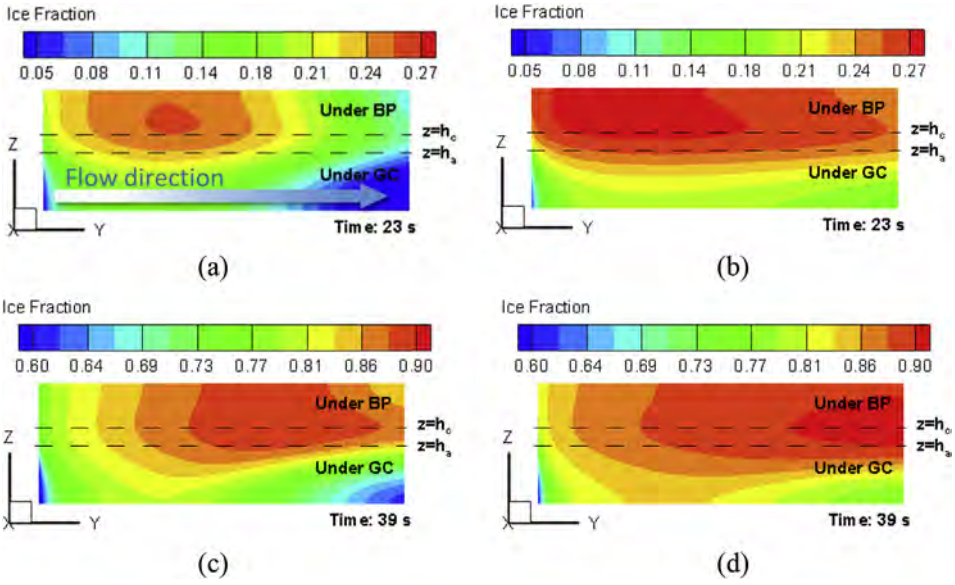

Fig. 8 – Ice fraction distribution in $x = 0.643$ mm plane (in CCL). (a) 20 LPM, −20 °C; (b) 80 LPM, −20 °C; (c) 20 LPM, −30 °C; (d) 40 LPM, −30 °C.

Summary and conclusion

In this work, the effects of coolant circulation on PEMFC cold start performances are investigated. For this purpose, a transient three-dimensional computational model including coolant circulation was developed based on the multi-disciplinary coupling governing equations. The cell voltage curve predicted by the model was validated against the experimental data, and the convergence of energy and water conservation equations were examined by heat and water balance calculations. The validated model was then used to run a parametric study. The cell voltage and temperature variation under different circulation parameters or different initial startup temperature are studied.

The results show that the coolant flow rate as well as the coolant tank capacity have negligible effects on cell voltage, but the temperature distribution is more uniform with higher flow rate or lower coolant tank capacity. Meanwhile the start-up process is prolonged obviously with higher coolant flow rate. At lower ambient temperatures, the PEMFC is more difficult to start up and the non-uniformity of the temperature distribution increases. Our analysis of the current density and ice formation showed that the temperature difference along flow direction significantly affects the electrochemical reaction intensity as the MEA properties are functions of temperature. With a more uniform temperature distribution under high coolant flow rate, the current density and ice fraction are also distributed more evenly, whereas the maximum ice fraction is larger. Besides, the ambient temperature shows great impacts on the ice accumulation position and the total ice formation amount.

Acknowledgements

Financial support received from the Natural Science Foundation of Guangdong Province (2017A000310186) and the Shanghai Automotive Industry Science and Technology Development Foundation (1706) is gratefully acknowledged. The author (LW) would also like to thank Prof. Kamel Hooman who is an awardee of the CAS PIFI Visiting Scientist Fellowship (2018VEB0003) for helpful discussion and instruction.

REFERENCES

[1] Myung S-T, Maglia F, Park K-J, Yoon CS, Lamp P, Kim S-J, Sun Y-K. Nickel-rich layered cathode materials for automotive lithium-ion batteries: achievements and perspectives. ACS Energy Letters 2016;2:196–223.
[2] Jiang J, Ruan H, Sun B, Wang L, Gao W, Zhang W. A low-temperature internal heating strategy without lifetime reduction for large-size automotive lithium-ion battery pack. Appl Energy 2018;230:257–66.
[3] Nair JR, Colò F, Kazzazi A, Moreno M, Bresser D, Lin R, Bella F, Meligrana G, Fantini S, Simonetti E, Appetecchi GB, Passerini S, Gerbaldi C. Room temperature ionic liquid (RTIL)-based electrolyte cocktails for safe, high working potential Li-based polymer batteries. J Power Sources 2019;412:398–407.
[4] Luo Y, Jiao K. Cold start of proton exchange membrane fuel cell. Prog Energy Combust 2018;64:29–61.
[5] Xie X, Zhang G, Zhou J, Jiao K. Experimental and theoretical analysis of ionomer/carbon ratio effect on PEM fuel cell cold start operation. Int J Hydrogen Energy 2017;42:12521–30.
[6] Yang Z, Du Q, Huo S, Jiao K. Effect of membrane electrode assembly design on the cold start process of proton exchange membrane fuel cells. Int J Hydrogen Energy 2017;42:25372–87.
[7] Meng H. Numerical analyses of non-isothermal self-start behaviors of PEM fuel cells from subfreezing startup temperatures. Int J Hydrogen Energy 2008;33:5738–47.
[8] Ko J, Ju H. Comparison of numerical simulation results and experimental data during cold-start of polymer electrolyte fuel cells. Appl Energy 2012;94:364–74.
[9] Luo Y, Jiao K, Jia B. Elucidating the constant power, current and voltage cold start modes of proton exchange membrane fuel cell. Int J Heat Mass Transf 2014;77:489–500.
[10] Tabe Y, Saito M, Fukui K, Chikahisa T. Cold start characteristics and freezing mechanism dependence on start-up temperature in a polymer electrolyte membrane fuel cell. J Power Sources 2012;208:366–73.
[11] Li L, Wang S, Yue L, Wang G. Cold-start icing characteristics of proton-exchange membrane fuel cells. Int J Hydrogen Energy 2019;44:12033–42.
[12] Ge S, Wang C-Y. Characteristics of subzero startup and water/ice formation on the catalyst layer in a polymer electrolyte fuel cell. Electrochim Acta 2007;52:4825–35.
[13] Bégot S, Harel F, Kauffmann JM. Experimental studies on the influence of operational parameters on the cold start of a 2 kW fuel cell. Fuel Cells 2008;8:138–50.
[14] Schießwohl E, von Unwerth T, Seyfried F, Brüggemann D. Experimental investigation of parameters influencing the freeze start ability of a fuel cell system. J Power Sources 2009;193:107–15.
[15] Ko J, Kim W, Hong T, Kim D, Ju H. Impact of metallic bipolar plates on cold-start behaviors of Polymer Electrolyte Fuel Cells (PEFCs). Solid State Ionics 2012;225:260–7.
[16] Khandelwal M, Lee S, Mench MM. One-dimensional thermal model of cold-start in a polymer electrolyte fuel cell stack. J Power Sources 2007;172:816–30.
[17] Konno N, Mizuno S, Nakaji H, Ishikawa Y. Development of compact and high-performance fuel cell stack. SAE Int J Alternat Powertrains 2015;4:123–9.
[18] Jiang F, Wang C-Y. Potentiostatic start-up of PEMFCs from subzero temperatures. J Electrochem Soc 2008;155:B743–51.
[19] Jiang F, Wang C-Y, Chen KS. Current ramping: a strategy for rapid start-up of PEMFCs from subfreezing environment. J Electrochem Soc 2010;157:B342–7.
[20] Du Q, Jia B, Luo Y, Chen J, Zhou Y, Jiao K. Maximum power cold start mode of proton exchange membrane fuel cell. Int J Hydrogen Energy 2014;39:8390–400.
[21] Gwak G, Ju H. A rapid start-up strategy for polymer electrolyte fuel cells at subzero temperatures based on control of the operating current density. Int J Hydrogen Energy 2015;40:11989–97.
[22] Sundaresan M, Moore RM. Polymer electrolyte fuel cell stack thermal model to evaluate sub-freezing startup. J Power Sources 2005;145:534–45.
[23] Tang T, Heinke S, Thüring A, Tegethoff W, Köhler J. A spatially resolved fuel cell stack model with gas–liquid slip phenomena for cold start simulations. Int J Hydrogen Energy 2017;42:15328–46.
[24] Zhu Y, Lin R, Jiang Z, Zhong D, Wang B, Shangguan W, Han L. Investigation on cold start of polymer electrolyte membrane fuel cells with different cathode serpentine flow fields. Int J Hydrogen Energy 2019;44:7505–17.

[25] Siegel C. Review of computational heat and mass transfer modeling in polymer-electrolyte-membrane (PEM) fuel cells. Energy 2008;33:1331–52.
[26] Jiang F, Fang W, Wang C-Y. Non-isothermal cold start of polymer electrolyte fuel cells. Electrochim Acta 2007;53:610–21.
[27] Yao L, Peng J, Zhang J-b, Zhang Y-j. Numerical investigation of cold-start behavior of polymer electrolyte fuel cells in the presence of super-cooled water. Int J Hydrogen Energy 2018;43:15505–20.
[28] Jiang F, Wang CY. Numerical modeling of liquid water motion in a polymer electrolyte fuel cell. Int J Hydrogen Energy 2014;39:942–50.
[29] Wang CY. Fundamental models for fuel cell engineering. Chem Rev 2004;104:4727–66.
[30] Springer TE, Zawodzinski TA, Gottesfeld S. Polymer electrolyte fuel cell model. J Electrochem Soc 1991;138:2334–42.
[31] Mao L, Wang CY. Analysis of cold start in polymer electrolyte fuel cells. J Electrochem Soc 2007;154:B139–46.
[32] Mao L, Wang C-Y, Tabuchi Y. A multiphase model for cold start of polymer electrolyte fuel cells. J Electrochem Soc 2007;154:B341–51.
[33] Motupally S, Becker AJ, Weidner JW. Diffusion of water in Nafion 115 membranes. J Electrochem Soc 2000;147:3171–7.
[34] Wang F. -20 °C cold start of fuel cell engine. Shanghai Auto 2017:3–6 (in Chinese).
[35] Asghari S, Akhgar H, Imani BF. Design of thermal management subsystem for a 5 kW polymer electrolyte membrane fuel cell system. J Power Sources 2011;196:3141–8.
[36] Asensio FJ, San Martin JI, Zamora I, Onederra O. Model for optimal management of the cooling system of a fuel cell-based combined heat and power system for developing optimization control strategies. Appl Energy 2018;211:413–30.